

Potent and specific Atg8-targeting autophagy inhibitory peptides from giant ankyrins

Jianchao Li^{1,6}, Ruichi Zhu^{1,6}, Keyu Chen¹, Hui Zheng^{2,3}, Hongyu Zhao^{2,3}, Chongzhen Yuan^{2,3}, Hong Zhang^{2,3*}, Chao Wang^{1,4*} and Mingjie Zhang^{1,5*}

The mammalian Atg8 family proteins are central drivers of autophagy and contain six members, classified into the LC3 and GABARAP subfamilies. Due to their high sequence similarity and consequent functional overlaps, it is difficult to delineate specific functions of Atg8 proteins in autophagy. Here we discover a super-strong GABARAP-selective inhibitory peptide harbored in 270/480 kDa ankyrin-G and a super-potent pan-Atg8 inhibitory peptide from 440 kDa ankyrin-B. Structural studies elucidate the mechanism governing the Atg8 binding potency and selectivity of the peptides, reveal a general Atg8-binding sequence motif, and allow development of a more GABARAP-selective inhibitory peptide. These peptides effectively blocked autophagy when expressed in cultured cells. Expression of these ankyrin-derived peptides in *Caenorhabditis elegans* also inhibited autophagy, causing accumulation of the p62 homolog SQST-1, delayed development and shortened life span. Thus, these genetically encodable autophagy inhibitory peptides can be used to occlude autophagy spatiotemporally in living animals.

Autophagy is an evolutionarily conserved degradation system in eukaryotes^{1,2}. It is responsible for degrading intracellular protein aggregates, damaged organelles and invasive pathogens, and thus is essential in maintaining cellular homeostasis as well as responding to stress conditions^{3–5}. Dysregulation of autophagy is associated with a variety of human diseases, including but not limited to cancers, metabolic diseases, immune disorders and neurodegenerative diseases^{6–9}.

Genetic screens in yeast and *C. elegans* have enabled researchers to identify and characterize a series of key components of the autophagy machinery, including autophagy-related (*Atg*) genes and ectopic P granules (*Epg*) genes^{4,10–14}. Among these autophagy proteins, Atg8 participates in multiple steps of the autophagic process^{15–17}. Atg8 attaches to the phagophore membrane via conjugation with phosphatidylethanolamine^{18,19}. Atg8–phosphatidylethanolamine can promote phagophore elongation and closure^{17,20,21}. Atg8 also recruits the Atg1–ULK1 complex to the phagophore to promote autophagosome formation²². In the closed autophagosome, Atg8 on the outer membrane interacts with Rab effectors PLEKHM1 and EPG5 for fusion with late the endosome or lysosome^{23,24}. In selective autophagy, Atg8 on the inner membrane of the phagophore interacts with autophagy receptors (for example, p62 and NBR1) to recruit targets for degradation^{25,26}. As a result, Atg8 and its orthologs (Atg8s) are commonly used as autophagy indicators^{27,28}, and elimination of Atg8 function impairs autophagy. Yeast contains only one *Atg8*, but in higher eukaryotes such as *C. elegans*, there are two homologs, *LGG-1* and *LGG-2*. In vertebrates, these two members further expand into two subfamilies, namely the GABARAP subfamily (GABARAPs, including GABARAP, GABARAPL1 and GABARAPL2) and the LC3 subfamily (LC3s, including LC3A, LC3B and LC3C)¹⁵. The two families have some non-redundant functions, and neither of them is dispensable for the overall autophagic

process^{20,21,29}. However, the high sequence similarities shared by mammalian Atg8 homologs and potential genetic compensation complicate functional studies of each individual member.

Atg8s contain a short N-terminal two-helix extension followed by a C-terminal ubiquitin-like domain. Atg8s can recognize proteins containing a Φ XX Ψ motif (where Φ represents tryptophan, tyrosine or phenylalanine, Ψ represents leucine, isoleucine or valine, and X represents any amino acid), also known as the LC3 interacting region (LIR) or Atg8 interacting motif^{30,31}. In addition to the aromatic and the hydrophobic residues, a typical LIR usually contains a few N-terminal acidic residues and binds to Atg8s with modest K_d values ranging from micromolar to submicromolar. Two recent studies have reported the development of LIR-based sensors to monitor autophagy using different strategies^{32,33}. However, these LIR-based peptides also bind to Atg8s with modest affinities. Due to the central roles of Atg8s in autophagy, it is highly desirable to develop potent and selective Atg8-binding peptides for applications such as inhibiting Atg8-mediated autophagy spatiotemporally in living animals, delineating functions of different Atg8 members in autophagy, and monitoring autophagy by specifically recognizing each member of the Atg8 family. We have noted that the 480 kDa ankyrin-G (AnkG), a neuron-specific isoform of AnkG^{34,35}, was recently reported to bind to GABARAP with $K_d \approx 10\text{--}20\text{ nM}$ ³⁶. The superior affinity of the binding between AnkG and GABARAP prompted us to ask whether it might be possible to develop super-strong Atg8-binding peptides as autophagy inhibitors.

We found that an extended AnkG-LIR peptide could bind to GABARAP with a super-strong affinity ($K_d \approx 2.6\text{ nM}$). Notably, this AnkG-LIR peptide binds to the LC3 subfamily with substantially weaker affinity. High-resolution crystal structures of AnkG-LIR in complex with GABARAPL1 or LC3B reveal the molecular basis for the super-strong and selective binding of AnkG-LIR to GABARAP.

¹Division of Life Science, State Key Laboratory of Molecular Neuroscience, Hong Kong University of Science and Technology, Clear Water Bay, Kowloon, Hong Kong, China. ²National Laboratory of Biomacromolecules, CAS Center for Excellence in Biomacromolecules, Institute of Biophysics, Chinese Academy of Sciences, Beijing, China. ³College of Life Sciences, University of Chinese Academy of Sciences, Beijing, China. ⁴Hefei National Laboratory for Physical Sciences at the Microscale, School of Life Sciences, University of Science and Technology of China, Hefei, Anhui, China. ⁵Center of Systems Biology and Human Health, Institute for Advanced Study, Hong Kong University of Science and Technology, Clear Water Bay, Kowloon, Hong Kong, China. ⁶These authors contributed equally: Jianchao Li, Ruichi Zhu. *e-mail: hongzhang@sun5.ibp.ac.cn; cwangust@ustc.edu.cn; mzhang@ust.hk

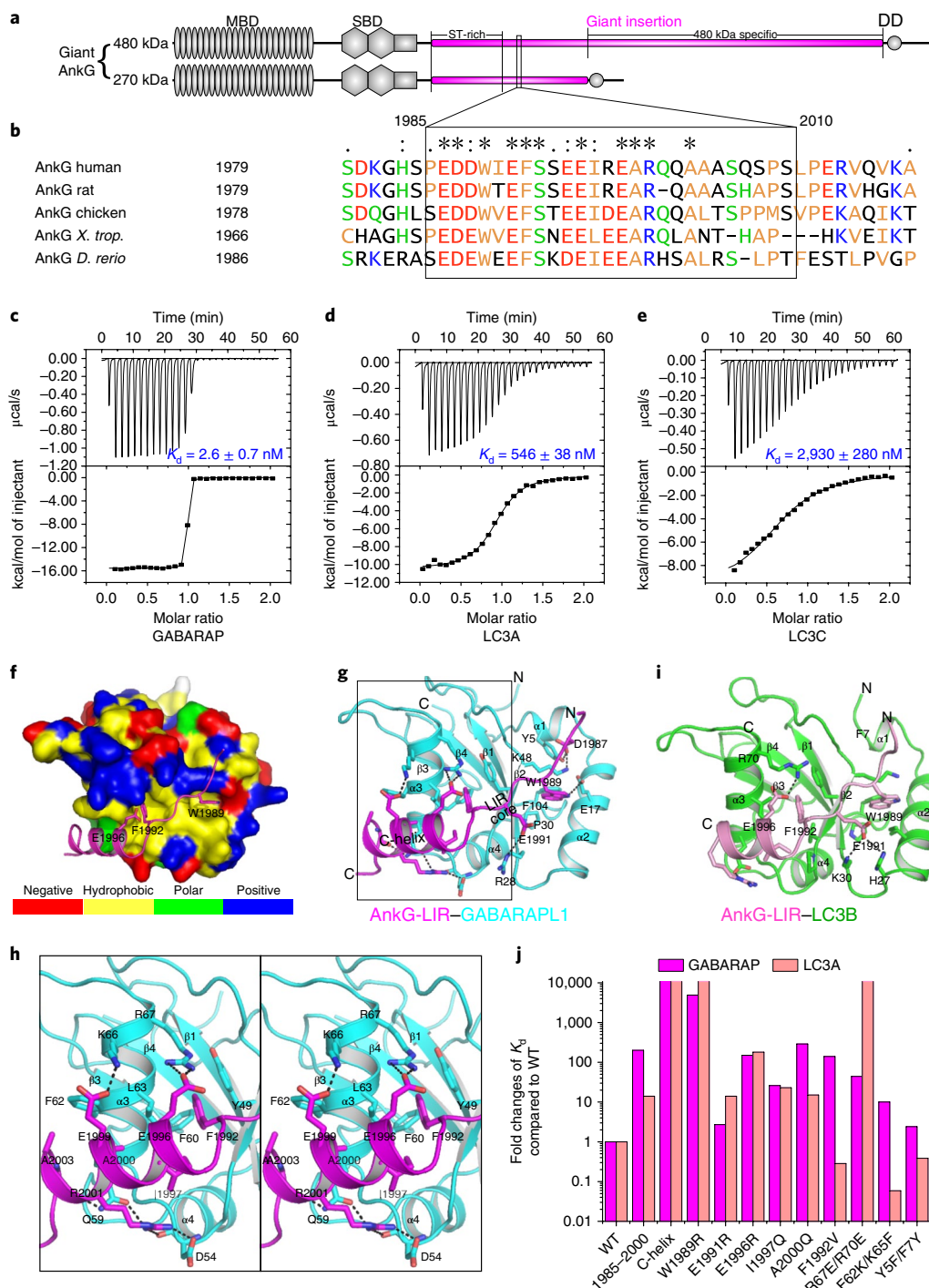


Fig. 1 | The super-strong affinity of selective AnkG-LIR binding to GABARAPs and its structural basis. a, Domain organizations of 270/480 kDa AnkG and the location of the LIR sequence in AnkG. MBD, Membrane Binding Domain, SBD, Spectrin Binding Domain, DD, Death Domain. **b**, Sequence alignment of AnkG-LIR from vertebrates. *X. trop.*, *Xenopus tropicalis*; *D. rerio*, *Danio rerio*. The symbols above the sequences are defined as follows: an asterisk (*) indicates positions that have a single, fully conserved residue; a colon (:) indicates conservation between groups of strongly similar properties; a period (.) indicates conservation between groups of weakly similar properties. **c–e**, ITC results for GABARAP (**c**), LC3A (**d**) and LC3C (**e**), showing that AnkG-LIR can bind to GABARAP with nanomolar affinities and to LC3s with affinities ranging from hundreds to thousands of nM; see Supplementary Fig. 2. ITC profiles are representative of three independent experiments (see Supplementary Fig. 1). The ITC-derived dissociation constants here and throughout the manuscript are reported as value \pm fitting errors. **f**, Combined surface (GABARAPL1) and ribbon-stick (AnkG-LIR) model showing the two hydrophobic pockets of GABARAPL1 accommodating the LIR core and the C-helix of AnkG-LIR. **g**, Ribbon representation of the AnkG-LIR-GABARAPL1 complex structure. Key residues critical for the binding are shown in stick model format. Salt bridges and hydrogen bonds are indicated with dashed lines. **h**, Stereo view showing the detailed interactions of the AnkG-LIR C-helix and GABARAPL1. **i**, Ribbon representation of the AnkG-LIR-LC3B complex structure. Key residues critical for binding are shown in stick model format. **j**, Bar graph showing the impacts on binding resulted from truncations or mutations of critical residues in the interface. Titrations for WT and WR mutant were performed three times; others were performed once. K_d values are reported in Supplementary Table 2.

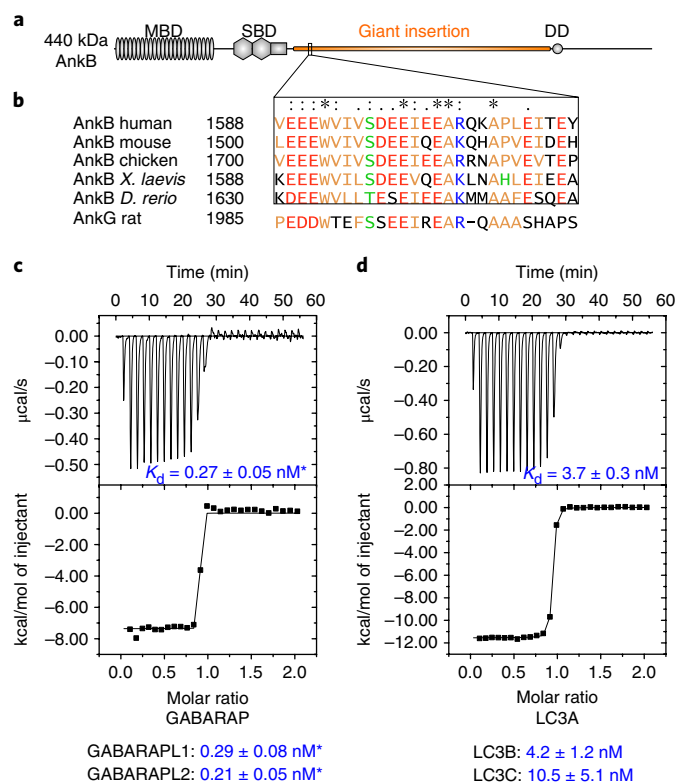


Fig. 2 | AnkB-LIR binds to all Atg8 family members with super-strong affinities. **a**, Domain organizations of 440 kDa AnkB and the locations of the extended LIR sequence, which is found only in the giant AnkB isoform. MBD, membrane binding domain; SBD, spectrin binding domain; DD, death domain. **b**, Sequence alignment of AnkB-LIR in vertebrates. AnkG-LIR is also included as a reference. *X. laevis*, *Xenopus laevis*; *D. rerio*, *Danio rerio*. **(c,d)** ITC results showing the super-strong binding of AnkB-LIR to every member of the Atg8 family. Asterisks indicate that K_d values were derived from competition-based ITC due to the super-strong binding. ITC profiles are representative of three independent experiments as described in Fig. 1. See Supplementary Fig. 4 for details.

We discovered that the 440 kDa neuron-specific isoform of ankyrin-B (AnkB) also contained an extended LIR motif. The AnkB-LIR peptide bound to all members of the Atg8 family with even higher affinities. The AnkB-LIR and AnkG-LIR (AnkB/G-LIR) peptides can function as potent and genetically encodable inhibitors of autophagy in living cells and in animals, and they may be used for developing methods of treating autophagy-related diseases.

Results

Giant AnkG preferentially binds to the GABARAP subfamily. The AnkG LIR motif identified earlier³⁶ is located in the N-terminal part of the giant insertion shared by the two giant AnkG isoforms (270/480 kDa AnkG) (Fig. 1a). We mapped the minimal GABARAP binding region of AnkG to a 26-amino acid peptide (residues 1985–2010, referred to as AnkG-LIR from here on), which is about 10 residues longer than known LIR sequences (Fig. 1b). This stretch of sequence is evolutionarily conserved in AnkG and binds to GABARAP with $K_d \approx 2.6$ nM by the isothermal titration calorimetry (ITC) assay (Fig. 1b,c and Supplementary Fig. 1a). The binding between AnkG and GABARAP is $\sim 1,000$ -fold stronger than almost all reported bindings between LIR motifs and Atg8s, qualifying AnkG-LIR as a super-strong GABARAP binder. AnkG-LIR can also bind to GABARAP1 with super-strong affinity ($K_d \approx 3.7$ nM) and to GABARAP2 with a somewhat lower affinity

($K_d \approx 40$ nM, Supplementary Fig. 2a,b). Surprisingly, AnkG-LIR binds to the LC3s with K_d values ranging from hundreds to thousands of nM (Fig. 1d,e and Supplementary Figs. 1b and 2c), indicating that AnkG-LIR can differentiate between the two subfamilies of Atg8s and selectively bind to the GABARAPs.

Structures of the AnkG-LIR/Atg8 complexes. To elucidate the molecular basis governing the super-strong and selective binding between AnkG-LIR and GABARAPs, we determined high-resolution crystal structures of AnkG-LIR in complex with GABARAP1 and with LC3B, respectively (Fig. 1f–i and Supplementary Table 1). The GABARAP1-bound AnkG-LIR is composed of two parts: the N-terminal extended structure formed by the LIR core containing the signature Φ XX Ψ motif and a C-terminal extension containing a three-turn α -helix (termed the C-helix; Glu1996 to Ala2003), which is missing in the reported LIRs (Fig. 1g,h). Essentially the interaction between the AnkG-LIR core and GABARAP1 is essentially the same as those between reported LIRs and all Atg8s^{16,30,31} (Fig. 1f,g). As expected, substitution of Trp1989 with arginine led to a marked weakening of the binding of AnkG-LIR to GABARAP or to LC3 (Fig. 1j and Supplementary Table 2). The C-helix extensively interacts with residues from $\alpha 3$ – $\alpha 4$ of GABARAP1 (Fig. 1h). Removal of half the C-helix from AnkG-LIR (the 1985–2000 construct) resulted in a ~ 200 -fold decrease of its binding to GABARAP (Fig. 1j). However, the AnkG-LIR C-helix alone (residues 1993–2010) has no detectable binding to GABARAP (Fig. 1j). Therefore, the synergistic actions of the canonical LIR motif and the C-helix confer on AnkG-LIR a super-strong binding to GABARAP. The binding interface between the C-helix and GABARAP1 $\alpha 3$ – $\alpha 4$ involves extensive hydrophobic and charge–charge interactions (Fig. 1h). Mutations of residues in the interaction interface invariably decreased the binding between AnkG-LIR and GABARAP (Fig. 1j).

The overall structure and the binding mode of the AnkG-LIR/LC3B complex are similar to that of AnkG-LIR/GABARAP1 (r.m.s. deviation of 0.86 Å; Fig. 1i). An important difference is that the LC3-bound AnkG-LIR C-helix is significantly shorter (covering only Glu1996–Arg2001), suggesting that the length of the C-helix is correlated with the strength of the binding with Atg8s (Fig. 1c,d). The shorter C-helix of AnkG-LIR is nevertheless also important for LC3 binding, as substitutions of the critical residues or truncating the C-helix decreased or even abolished AnkG-LIR's binding to LC3 (Fig. 1j). Notably, we observed that Glu1991 from AnkG interacts with Lys30 and His27 of LC3B whereas the same glutamate only weakly interacts with Arg28 of GABARAP1 (Fig. 1g,i). We predicted that substitution of Glu1991 with arginine would weaken AnkG-LIR's binding to LC3s but have limited impact on its binding to GABARAPs, so that the mutant AnkG-LIR might have even higher selectivity in binding to GABARAPs over LC3s. Indeed, the E1991R AnkG-LIR bound to GABARAP with a slightly weaker affinity but to LC3A with a ~ 10 -fold lower affinity, thereby increasing the selectivity between GABARAP and LC3A to $\sim 1,000$ -fold (Fig. 1j). We have also dissected the structural determinants for the selective binding of AnkG-LIR to GABARAPs over LC3s (Supplementary Fig. 3). To the best of our knowledge, these AnkG-LIR-derived peptides are the first highly selective and super-strong GABARAP binding peptides.

AnkB binds to all Atg8s with super-strong affinities. The super-strong binding of AnkG-LIR to GABARAP prompted us to search for other strong Atg8 binding proteins. A BLAST search using AnkG-LIR as the template against the human proteome returned a similar extended LIR sequence from the 440 kDa AnkB as the top candidate, and we refer it as AnkB-LIR (Fig. 2a,b). The 440 kDa AnkB is also a neuron-specific isoform, mainly expressed in unmyelinated or premyelinated axons³⁷. AnkB-LIR also contains a LIR core Φ XX Ψ followed by a stretch of amino acid residues with

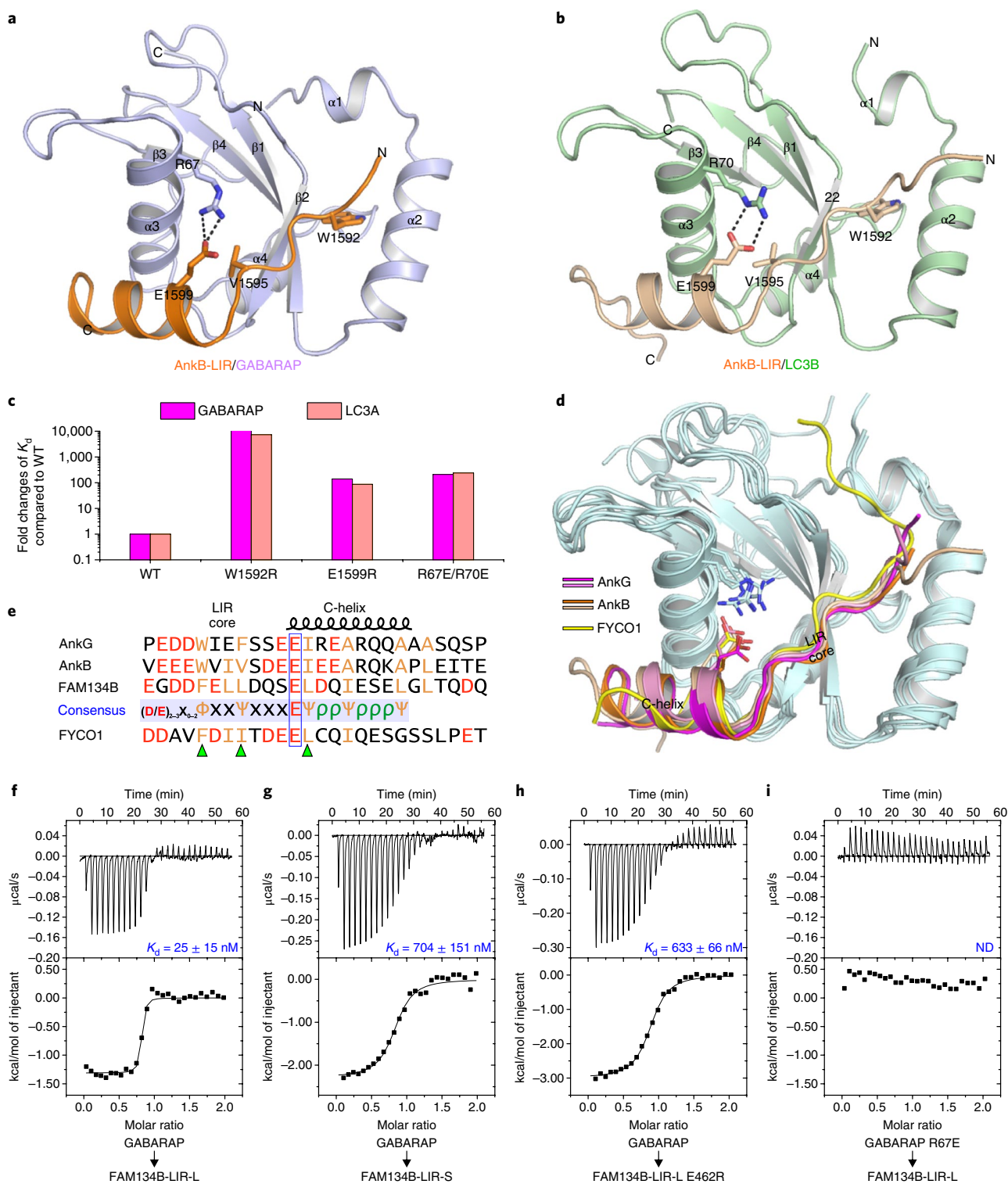


Fig. 3 | Structures of AnkB-LIR in complex with GABARAP and LC3B reveal a consensus sequence motif for the extended LIRs with strong binding to Atg8s. a, b, Ribbon diagram of the crystal structures of the AnkB-LIR-GABARAP (**a**) and AnkB-LIR-LC3B (**b**) complexes. The two hydrophobic residues in LIR core and the Glu1599^{AnkB}-Arg67 and Glu1599^{AnkB}-Arg70^{Atg8} salt bridges are highlighted in stick model format. **c**, Bar graph showing that mutations of the critical residues in the interface weakened the binding. K_d values are reported in Supplementary Table 2. Titrations for WT and WR mutant were performed three times; others were performed once. **d**, Superposition of the AnkG (magenta)-GABARAP1, AnkG (pink)-LC3B, AnkB (orange)-GABARAP, AnkB (light orange)-LC3B and FYCO1 (yellow)-LC3A (PDB: 5CX3) complex structures showing the common binding mode of Atg8s to the extended LIR sequences, consisting of the LIR core followed by the C-helix starting with glutamate. **e**, Sequence alignment of LIRs containing a LIR core together followed by an amphipathic C-helix. The consensus sequence D/E₂₋₃X₀₋₂ΦXXΨXXXEΨρρΨρρρΨ is also shown. **f, g**, ITC results (two independent experiments for each) showing that GABARAP binds to FAM134B-LIR with the C-helix extension much more strongly than that without the C-helix. **h, i**, ITC results (one experiment for each mutant) showing that charge reversal mutations of the predicted Glu462-Arg67 salt bridge weaken or even disrupt the binding between FAM134B and GABARAP. ND, not detectable.

limited homology with the AnkG-LIR C-helix (Fig. 2b). Nevertheless, the sequence of AnkB-LIR is highly conserved in the 440kDa AnkB throughout evolution (Fig. 2b). We found that AnkB-LIR bound to GABARAP with an affinity about tenfold higher than that of AnkG-LIR (K_d values of ~ 0.27 nM vs. 2.6 nM; Fig. 2c vs. Fig. 1c). Surprisingly, AnkB-LIR binds to all Atg8s with super-strong affinities (K_d values from 0.21 nM to 10.5 nM; Fig. 2c,d and Supplementary Fig. 4). The super-strong binding of AnkB-LIR to Atg8s qualifies the peptide as an alternative to antibodies against Atg8s (Supplementary Fig. 5).

Structures of the AnkB-LIR/Atg8s complexes. To understand the mechanisms governing the strong interactions between AnkB-LIR and Atg8s, we solved the crystal structures of the AnkB-LIR/GABARAP and AnkB-LIR/LC3B complexes (Fig. 3a,b and Supplementary Table 1). The overall structural features of the binding of AnkB-LIR to GABARAP and LC3B are highly similar to those of the binding of AnkG to GABARAP1 and LC3B (Fig. 3a,b), and AnkB-LIR also contains a well-defined C-helix following the LIR core. As expected again, substitution of Trp1592 (the first hydrophobic residue in the $\Phi XX\Psi$ LIR motif) by arginine dramatically decreased the binding of AnkB-LIR to all members of the human Atg8 family (Fig. 3c). Thus, this W1592R mutant of AnkB-LIR (AnkB WR) served as an ideal control for our functional studies of autophagy inhibition in cell cultures and in vivo below.

There are several subtle but significant differences when comparing the binding of AnkB-LIR and AnkG-LIR to the Atg8 members, which can explain why AnkB-LIR binds to Atg8s uniformly more strongly than AnkG-LIR does. The two middle residues in the $\Phi XX\Psi$ LIR motif of AnkB-LIR are also hydrophobic (Val1593 and Ile1594, corresponding to Thr1990 and Glu1991 in AnkG-LIR; Fig. 2b), and these two residues actively interact with a number of hydrophobic residues from GABARAP and LC3B (Supplementary Fig. 6). In AnkG-LIR, only Glu1991 engages in binding to LC3B (Fig. 1g,i). In the AnkB-LIR/LC3B complex, the side chain of Lys65 from LC3B forms hydrogen bonds with the backbone of two residues from the AnkB-LIR C-helix (Supplementary Fig. 6), providing an explanation to why Lys65 in the LC3 subfamily can favorably interact with AnkB-LIR but not with AnkG-LIR.

Extended LIR motif facilitates strong binding to Atg8. A defining feature for the strong Atg8 binding sequences from AnkB/G-LIRs revealed from the above structural studies is the presence of a ~ 10 -residue amphipathic α -helix (the C-helix) immediately following the canonical LIR motif (Fig. 3d,e). The interface areas of the super-strong extended LIR-Atg8 complexes (for example, GABARAP1-AnkG, GABARAP-AnkB and LC3B-AnkB) are substantially larger than those of canonical LIR-Atg8 complexes with intermediate affinities ($>800 \text{ \AA}^2$ vs. $500\text{--}700 \text{ \AA}^2$). A glutamate residue at the beginning of the C-helix forms a pair of salt bridges with an absolutely conserved arginine at the end of $\alpha 3$ in all Atg8s (Fig. 3d and Supplementary Fig. 3a). Three nonaromatic hydrophobic residues at the positions 1, 4 and 8 immediately following this glutamate residue are aligned on the same face of the C-helix and interact with the hydrophobic surface formed by $\alpha 3$ of Atg8s. We searched the human proteome for other super-strong Atg8 binders using the following criteria: existence of a canonical LIR motif immediately followed by a three-turn or longer amphipathic α -helix starting with a glutamate residue. Such a search returned several potential candidates. Among these, FAM134A, B and C (also known as reticulophagy regulators 2, 1 and 3, respectively) fit the search criteria particularly well (Fig. 3e). We tested the binding of GABARAP to human FAM134B-LIR with or without the C-helix extension (referred to respectively as LIR-L for residues 448–469 and LIR-S for 448–461). In agreement with our prediction, GABARAP bound to FAM134B-LIR-L with a very high affinity

($K_d \approx 25$ nM; Fig. 3f). Truncation of the predicted C-helix led to a marked decrease of its binding to GABARAP (K_d increased to 704 nM; Fig. 3g). Additionally, the charge reversal mutation of Glu462 in FAM134B (equivalent to Glu1996 in AnkG-LIR) or Arg67 in GABARAP led to decrease or even total disruption of the binding (Fig. 3h,i), suggesting that FAM134B adopts a similar binding mode to that of AnkB/G-LIRs. Taking all of the data together, we propose a consensus sequence motif for the extended LIRs with super-strong Atg8 binding affinities: $D/E_{2-3}X_{0-2}\Phi XX\Psi XXXE\Psi\rho\rho\Psi$, where Φ , Ψ , ρ , and X represent aromatic, aliphatic, polar, and any residues, respectively (Fig. 3e).

A recently identified LC3 binding sequence from FYCO1 has a feature partially fitting the super-strong Atg8 binding motif, having only a one-turn helix extension following the canonical LIR motif^{38,39} (Fig. 3d,e). Accordingly, the binding of FYCO1-LIR to LC3 is substantially weaker than the binding of AnkB-LIR to Atg8s.

AnkB/G-LIR peptides as potent autophagy inhibitors. Based on the above biochemical and structural studies, we expected that expression of AnkB wild-type LIR (AnkB WT; see Fig. 4a for peptide sequences) would eliminate all LIR-dependent target binding to every Atg8 member, whereas overexpression of AnkG E1991R LIR (AnkB ER) would selectively block LIR-dependent target binding to GABARAPs. Expression of AnkG WT would eliminate the binding of GABARAPs to their targets and may compromise the binding of LC3s to their targets to a certain degree. The AnkB/G WR peptides should have minimal impact on target binding to Atg8s and thus can be used as specific negative controls of the AnkB/G-LIR peptides in the autophagy inhibition assays below.

We used COS7 cells to assess autophagy inhibition by the AnkB/G-LIR peptides. We quantified the numbers of endogenous LC3- or GABARAP-positive puncta, which represent LC3- or GABARAP-containing autophagic structures, as readouts to quantify autophagy inhibition^{27,28}. After nutrient deprivation, obvious accumulations of LC3- or GABARAP-positive puncta could be observed in cells overexpressing mCherry only, indicating induction of autophagy (Fig. 4b–e and Supplementary Fig. 7a). Overexpression of mCherry-AnkB WT reduced the LC3 and GABARAP puncta to background levels. In contrast, expression of the mCherry-AnkB WR peptide had no impact on the number of LC3 or GABARAP puncta (Fig. 4c,e, Supplementary Fig. 7b,c). The above results indicate that the AnkB WT peptide can function as a potent autophagy inhibitor targeting all Atg8 family members. Electron microscopy revealed that cells expressing the AnkB WT peptide contained much fewer autophagosomes than cells expressing the AnkB WR peptide. Isolation membranes did not accumulate in cells expressing the AnkB WT peptide (Supplementary Fig. 8a–c). Expressions of markers for the autophagy initiating complex (for example, FIP200) and omegasome (for example, DFCEP1) were not affected (Supplementary Fig. 8d–f), while formation of LC3 puncta was inhibited (Fig. 4b,c). Additionally, in cells or worms overexpressing the AnkB peptide, levels of lipidated LC3 or LGG-1 remained largely unchanged (or only slightly increased), unlike a marked accumulation in mutants with defective autophagosome maturation, such as the *epg-5* mutant (Supplementary Fig. 8g,h and Supplementary Fig. 13). Together, the above results suggested that overexpression of the super-potent AnkB WT peptide blocks an early step in autophagy, before formation of isolation membranes.

Entirely consistent with our biochemical data, the AnkG WT peptide potentially inhibited GABARAP puncta formation but only modestly reduced LC3-positive puncta when overexpressed in COS7 cells (Fig. 4c,e and Supplementary Fig. 7b,c). The AnkG ER peptide had a minor impact on the reduction in the number of LC3 puncta, but potentially inhibited formation of GABARAP puncta (Fig. 4b–e), indicating that the AnkG ER peptide can indeed function as a specific GABARAP-mediated autophagy inhibitor. As a negative and

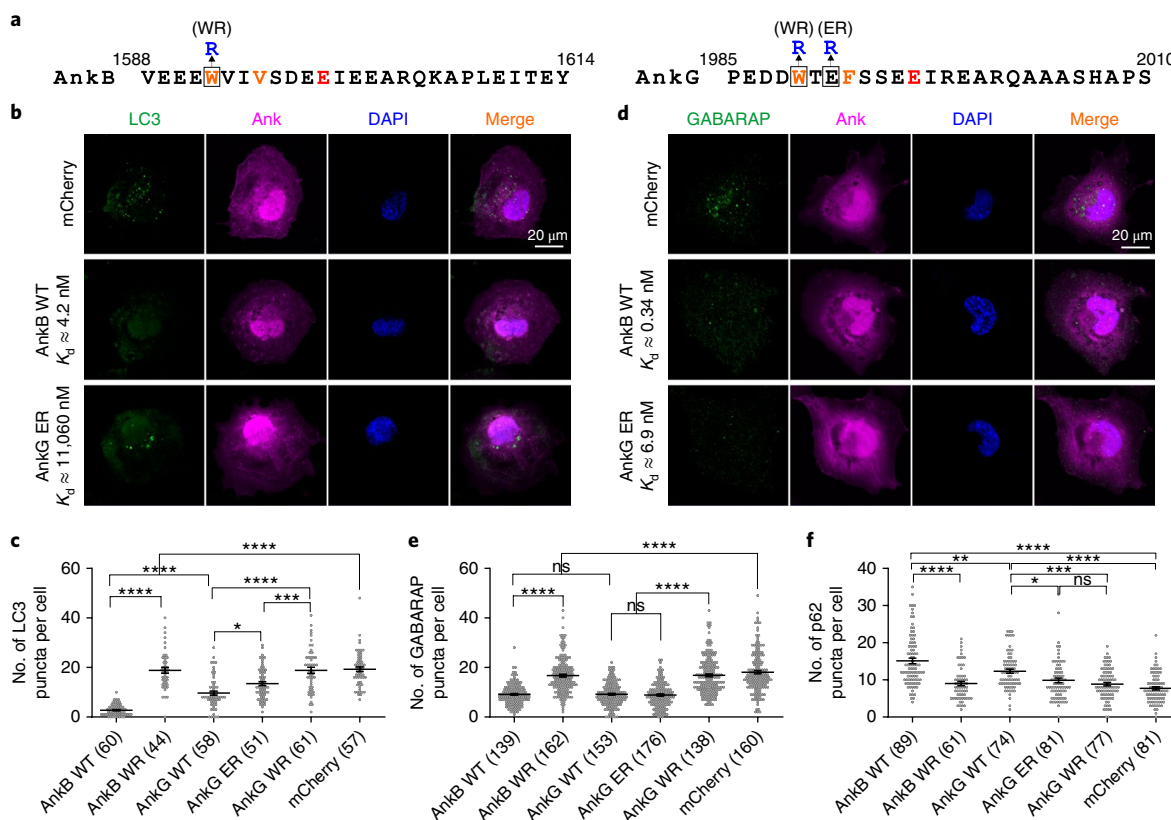


Fig. 4 | Autophagy inhibition by AnkB/G-LIR peptides in COS7 cells. **a**, Amino acid sequences of the AnkB/G peptides used in the cell culture here, as well as in *C. elegans* studies below. **b,d**, Representative images of the LC3-positive puncta (**b**) and GABARAP-positive puncta (**d**) in COS7 cells expressing different mCherry-tagged AnkB/G peptides. Top: mCherry only; middle: AnkB WT; bottom: AnkG ER. **c,e,f**, Quantification of the numbers of LC3-positive (**c**), GABARAP-positive (**e**) and p62-positive (**f**) puncta in COS7 cells expressing different mCherry-tagged AnkB/G peptides. Data are expressed as mean \pm s.e.m. and were analyzed with GraphPad Prism 6 using one-way ANOVA followed by Tukey's multiple comparisons test; ns: not significant, $P > 0.05$; $*P \leq 0.05$; $**P \leq 0.01$; $***P \leq 0.001$; $****P \leq 0.0001$. See Supplementary Figs. 7 and 9 for representative images of LC3- and GABARAP-positive puncta of AnkB WR, AnkG WT, AnkG WR groups and p62-positive puncta of all groups. Adjusted P values: for LC3-positive puncta: AnkB WT/AnkB WR, $P < 0.0001$; AnkB WT/AnkG WT, $P < 0.0001$; AnkB WT/mCherry, $P < 0.0001$; AnkG WT/AnkG ER, $P = 0.0234$; AnkG WT/AnkG WR, $P < 0.0001$; AnkG ER/AnkG WR, $P = 0.0004$; AnkG WT/mCherry, $P < 0.0001$. For GABARAP-positive puncta: AnkB WT/AnkB WR, $P < 0.0001$; AnkB WT/AnkG WT, $P = 1$; AnkB WT/mCherry, $P < 0.0001$; AnkG WT/AnkG ER, $P = 0.9986$; AnkG WT/AnkG WR, $P < 0.0001$; AnkG ER/AnkG WR, $P = 0.0004$; AnkG WT/mCherry, $P < 0.0001$. For p62-positive puncta: AnkB WT/AnkB WR, $P < 0.0001$; AnkB WT/AnkG WT, $P = 0.0080$; AnkB WT/mCherry, $P < 0.0001$; AnkG WT/AnkG ER, $P = 0.0403$; AnkG WT/AnkG WR, $P < 0.0004$; AnkG ER/AnkG WR, $P = 0.8043$; AnkG WT/mCherry, $P < 0.0001$. The numbers of cells obtained from three or more batches of experiments are indicated in parentheses in the figure.

specificity control, we did not see any noticeable changes in the number of LC3 or GABARAP puncta in cells overexpressing the AnkG WR peptide (Fig. 4c,e and Supplementary Fig. 7b,c).

We further quantified the level of p62 to monitor the autophagic flux in COS7 cells expressing various AnkB/G-LIR peptides under starvation^{27,28}. Only a relatively low and steady level of p62 aggregates is formed if autophagic flux is normal²⁵, and this is indeed the case when cells were transfected with the mCherry vector control (Supplementary Fig. 9). Overexpression of the AnkB WT peptide dramatically increased the p62-positive puncta (Supplementary Fig. 9 and Fig. 4f), presumably due to the potent inhibition of all Atg8-mediated autophagy processes. Notably, although the AnkG WT peptide also obviously increased p62-positive puncta in COS7 cells, the increase was nevertheless significantly lower than that induced by the AnkB WT peptide (Fig. 4f), indicating that a portion of LC3-subfamily-mediated autophagy was not blocked by the AnkG WT peptide. Neither of the AnkB/G WR peptides could induce p62-positive puncta increase (Supplementary Fig. 9 and Fig. 4f). As expected, there was no statistically significant increase of p62-positive puncta

in cells expressing the AnkG ER peptide compared to the cells expressing mCherry or AnkB/G WR (Supplementary Fig. 9 and Fig. 4f). This is consistent with a previous siRNA-based study showing that knockdown of LC3 but not GABARAP causes p62 accumulation in COS7 cells⁴⁰. Taken together, the above cell-based assays reinforce our earlier conclusion derived from biochemical and structural studies that the AnkB WT peptide can function as potent autophagy inhibitor by targeting all members of the Atg8 family and the AnkG WT or ER peptides can selectively target GABARAPs and spare LC3s.

AnkB peptide expression impairs autophagy in *C. elegans*. *C. elegans* contain two *Atg8* genes, *lgg-1* and *lgg-2*, which encodes mammalian orthologs of GABARAP and LC3, respectively. *lgg-1* and *lgg-2* act non-redundantly in autophagy²¹. We measured the binding of various AnkB/G-LIR peptides to purified LGG-1 and LGG-2, using the same method as described for Figs 1 and 2. As with mammalian Atg8s, the AnkB WT peptide bound very strongly to both LGG-1 and LGG-2, and the WR mutation eliminated the binding (Supplementary Table 3). The AnkG WT peptide bound strongly

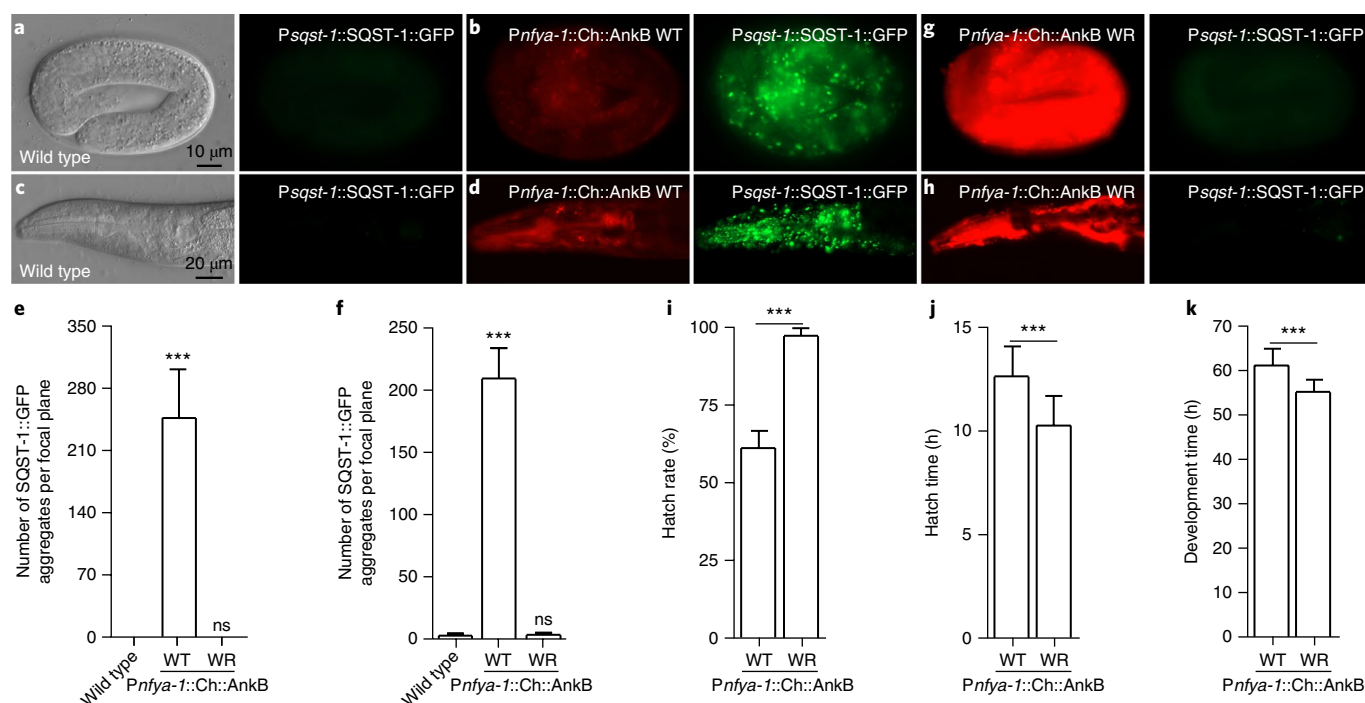


Fig. 5 | Expression of the AnkB peptide impairs autophagy in *C. elegans*. **a**, In wild-type embryos, SQST-1::GFP is weakly expressed and diffusely localized in the cytoplasm (right). Differential interference contrast image is shown at left. **b,g**, A large number of SQST-1::GFP aggregates accumulate in embryos expressing Cherry (Ch)::AnkB WT (**b**), but not in embryos expressing Ch::AnkB WR (**g**). **c**, In wild-type larvae, SQST-1::GFP is weakly expressed and diffusely localized in the cytoplasm (right). Differential interference contrast image is shown at left. **d,h**, Expression of the AnkB WT peptide (**d**), but not AnkB WR peptide (**h**), results in accumulation of SQST-1::GFP aggregates at the larval and adult stages. SQST-1::GFP aggregates in the head region are shown in **c,d,h**. Scale bars: 10 μ m (**a,b,g**) and 20 μ m (**c,d,h**). **e**, Quantification of the number of SQST-1::GFP aggregates per focal plane of embryos. Five independent embryos for each strain were quantified. Data are shown as mean \pm s.d. Two-tailed unpaired Student's *t*-test: $P=1.94 \times 10^{-5}$ (wild-type vs. embryos expressing Ch::AnkB WT), $P=1$ (wild-type vs. embryos expressing Ch::AnkB WR). ns: not significant, $P>0.05$; $***P \leq 0.001$. **f**, Quantification of the number of SQST-1::GFP aggregates per focal plane ($n=5$ for each strain) in the head region of L4 larvae. Five independent worms for each strain were quantitated. Data are shown as mean \pm s.d.; two-tailed unpaired Student's *t*-test: $P=6.73 \times 10^{-8}$ (wild-type vs. embryos expressing Ch::AnkB WT), $P=0.50$ (wild-type vs. embryos expressing Ch::AnkB WR). ns: not significant, $P>0.05$; $***P \leq 0.001$. **i**, Hatch rate of embryos expressing *Pnfy-1*::Ch::AnkB WT (BWT; $n=236$) and *Pnfy-1*::Ch::AnkB WR (BWR; $n=207$). Data are shown as mean \pm s.d., $P=1.96 \times 10^{-5}$, $***P \leq 0.001$. **j**, Time for embryos expressing *Pnfy-1*::Ch::AnkB WT ($n=13$) and *Pnfy-1*::Ch::AnkB WR ($n=14$) to develop into L1 larvae. Data are shown as mean \pm s.d.; $P=0.00028$, $***P \leq 0.001$. **k**, Time for L1 larvae expressing *Pnfy-1*::Ch::AnkB WT ($n=13$) and *Pnfy-1*::Ch::AnkB WR ($n=14$) to develop into young adults. Data are shown as mean \pm s.d., $P=7.46 \times 10^{-5}$, $***P \leq 0.001$.

to LGG-1 but with an ~ 130 -fold weaker affinity toward LGG-2. The AnkG ER peptide retained strong binding to LGG-1 and displayed $\sim 1,000$ -fold weaker binding to LGG-2 (Supplementary Table 3).

We next determined whether the AnkB WT peptide could block autophagy in *C. elegans*. Autophagy is required for degradation of the *C. elegans* p62 homolog SQST-1 during development¹⁴. In wild-type animals, SQST-1::GFP is weakly expressed and diffusely localized in the cytoplasm, while numerous SQST-1 aggregates accumulate in autophagy mutants¹⁴. We expressed the AnkB WT peptide fused with the Cherry reporter (Cherry::AnkB WT) or Cherry::AnkB WR under the control of the *nfy-1* promoter (*Pnfy-1*), which is expressed ubiquitously from embryonic to adult stages. Animals expressing Cherry::AnkB WT accumulated a large number of SQST-1::GFP aggregates in multiple tissues from the embryonic to adult stages (Fig. 5a–f). In contrast, no SQST-1::GFP aggregates formed in animals expressing Cherry::AnkB WR (Fig. 5e–h).

Autophagy plays critical roles in various physiological processes occurring during development or in adult *C. elegans*⁴¹. Fewer autophagy mutants develop into larvae⁴¹. Animals expressing *Pnfy-1*::Cherry::AnkB WT showed a significant reduction in hatching rate: 60.8% embryos expressing the AnkB WT peptide hatched, compared to 96.9% of embryos expressing AnkB WR (Fig. 5i). Autophagy

mutants also grow slowly⁴¹. Compared to embryos expressing AnkB WR mutant peptide, embryos expressing Cherry::AnkB WT took approximately 2 h more to develop into L1 larvae and 6 h more to develop into young adults (Fig. 5j,k). Thus, the AnkB WT peptide blocks autophagy during *C. elegans* development.

We similarly tested the blocking effect of AnkG peptides in *C. elegans*. Under control of the *y37A1B.5* promoter, Cherry::AnkG WT or ER peptides expressed in hypodermis, but not the Cherry::AnkG WR peptide, caused accumulation of SQST-1::GFP aggregates from embryonic to adult stages (Supplementary Fig. 10a–j). This observation is somewhat different from that in mammalian heterologous cells. This may be explained by the different roles of the two families in different organisms. In mammal, p62 degradation is dependent on LC3 but not GABARAP⁴⁰, so blocking GABARAP binding has minimal effect on p62 degradation. However, in *C. elegans*, LGG-1 acts upstream of LGG-2 and is essential for SQST-1 degradation^{21,29}.

AnkB peptide can spatiotemporally deplete autophagy. Although a large collection of autophagy mutants were isolated from genetic screens¹⁴, the available assays are not effective for inhibiting autophagy activity in a spatiotemporal manner (Supplementary Fig. 11). We investigated whether the AnkB peptide could block autophagy in a tissue- and time-specific manner. The AnkB peptide

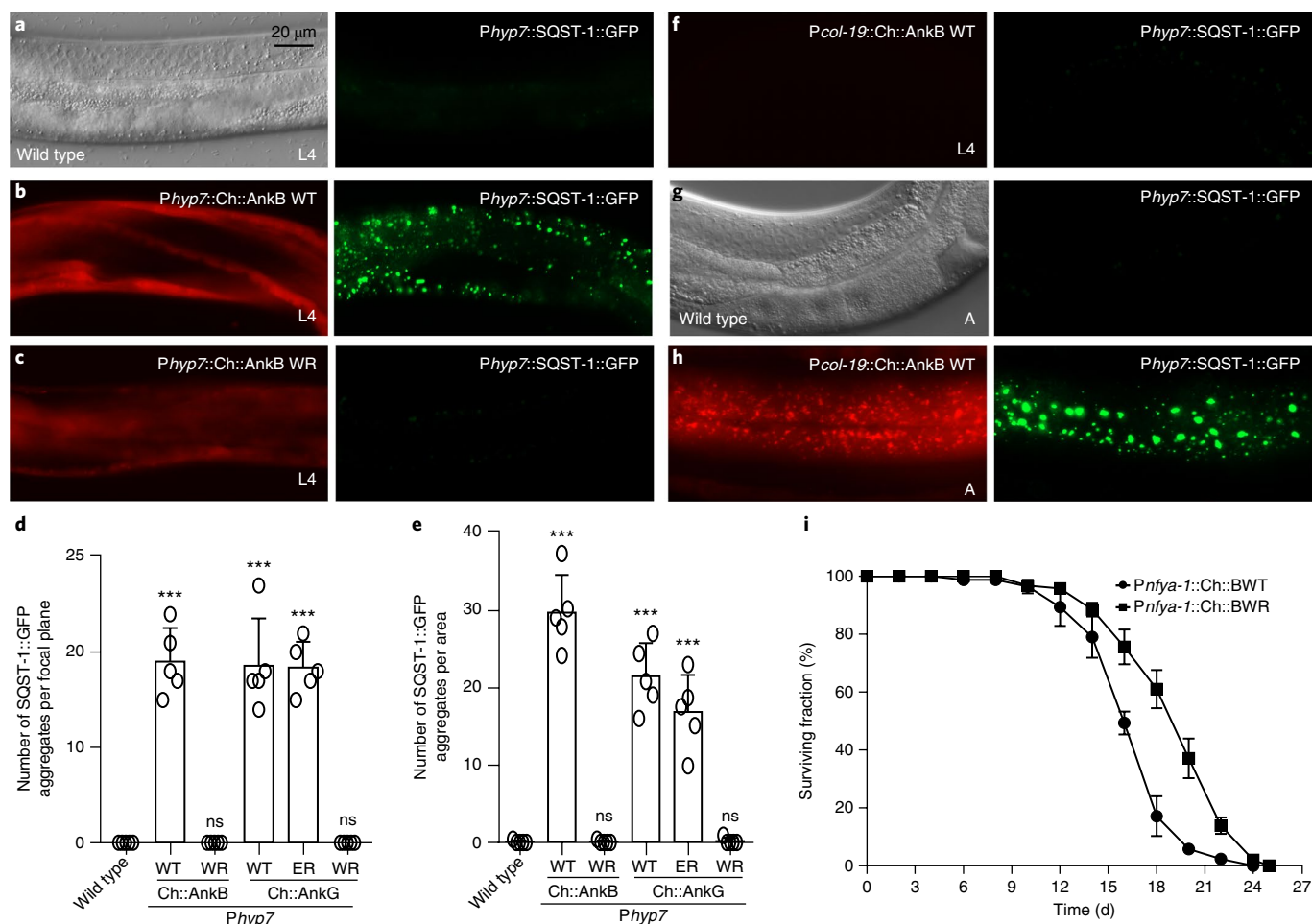


Fig. 6 | The AnkB peptide inhibits autophagy in a tissue- and time-specific manner. **a**, In wild-type animals carrying *bpls267*, SQST-1::GFP is weakly expressed and diffusely localized in hypodermis. **b,c**, Expression of the AnkB WT peptide (**b**), but not AnkB WR (**c**), results in accumulation of SQST-1::GFP aggregates in hypodermis at the larval and adult stages. **d**, Quantification of the number of SQST-1::GFP aggregates per focal plane in embryonic hypodermal cells expressing WT and mutant AnkB and AnkG peptide. Five independent embryos for each strain were quantified. Data are shown as mean \pm s.d. Two-tailed unpaired Student's *t*-test: $P = 2.12 \times 10^{-6}$ (wild-type vs. embryos expressing Cherry (Ch)::AnkB WT), $P = 1$ (wild-type vs. embryos expressing Ch::AnkB WR), $P = 2.97 \times 10^{-5}$ (wild-type vs. embryos expressing Ch::AnkG WT), $P = 3.43 \times 10^{-7}$ (wild-type vs. embryos expressing Ch::AnkG ER), $P = 1$ (wild-type vs. embryos expressing Ch::AnkG WR); ns: not significant, $P > 0.05$; *** $P \leq 0.001$. **e**, Quantification of the number of SQST-1::GFP aggregates per 1,000 μm^2 in hypodermal cells of L4 larvae. Five independent worms for each strain were quantified. Data are shown as mean \pm s.d., two-tailed unpaired Student's *t*-test: $P = 7.75 \times 10^{-7}$ (wild-type vs. worms expressing Ch::AnkB WT), $P = 0.9699$ (wild-type vs. worms expressing Ch::AnkB WR), $P = 4.00 \times 10^{-6}$ (wild-type vs. worms expressing Ch::AnkG WT), $P = 5.35 \times 10^{-5}$ (wild-type vs. worms expressing Ch::AnkG ER), $P = 0.6558$ (wild-type vs. worms expressing Ch::AnkG WR); ns: not significant, $P > 0.05$; *** $P \leq 0.001$. **f-h**, Expression of AnkB WT driven by the *col-19* promoter, which is specifically expressed at the adult stage in hypodermis, causes accumulation of SQST-1::GFP in adults (**g,h**), but not in L4 larvae (**f**). L4: L4 stage larvae; A: adults. Scale bars, 20 μm (**a-c,f-h**). **i**, Survival curves of *Pnfy-1::ch::AnkB* WT and *Pnfy-1::ch::AnkB* WR animals. Data are shown as mean \pm s.e.m. ($n = 5$ plates for each group in every batch of experiment). The experiments were repeated three times. Median life span is 16.32 d for animals expressing *Pnfy-1::ch::AnkB* WT and 19.15 d for animals expressing *Pnfy-1::ch::AnkB* WR; $P = 0.0000$. See Supplementary Table 4.

was expressed under the control of tissue-specific promoters, including the promoter of *myo-3* for body wall muscle cells, *y37A1B.5* for hypodermal cells, and *vha-6* for intestinal cells. The expression constructs were injected into animals carrying the corresponding tissue-specific SQST-1::GFP expression integrated lines. A large number of SQST-1::GFP aggregates accumulated in animals expressing AnkB WT peptide in different tissues from embryonic to adult stages, while animals expressing WR peptide showed no accumulation (Fig. 6a–e and Supplementary Fig. 10k–x). The number of SQST-1 aggregates in animals expressing the AnkB peptide was comparable to that in null autophagy mutants (for example, Supplementary Fig. 11g,h). RNAi-mediated knockdown of autophagy genes, delivered by RNAi feeding, caused less severe defects (Supplementary Fig. 11a–f,i–k).

We also compared the accumulation of SQST-1::GFP aggregates in animals with different expression levels of AnkB WT. Animals with weak expression contained less SQST-1::GFP aggregates, and the number of SQST-1::GFP aggregates increased with expression level (Supplementary Fig. 12a–f,i,j).

We also examined whether the AnkB peptide could impair autophagy in a temporal control manner. When the expression of AnkB WT was driven by the promoter of *col-19*, which is expressed in hypodermal cells from the young adult stage onward, animals exhibited adult-specific accumulation of SQST-1::GFP aggregates, while no aggregates were found from the embryonic to L4 larval stages (Fig. 6f–h).

Autophagy is known to regulate the worm life span. We found that worms expressing *Pnfy-1::Cherry::AnkB* WT had a markedly

shorter life span than animals expressing Cherry::AnkB WR (Fig. 6i). Expressing Cherry::AnkB WT in muscle cells and intestinal cells did not noticeably reduce the life span compared to that of animals expressing Cherry::AnkB WR (Supplementary Fig. 10y, left and right). Depleting autophagy activity in hypodermal cells by expressing Cherry::AnkB WT slightly reduced the mean life span (Supplementary Fig. 10y, middle). These results indicate that impairments of autophagy in different tissues contribute differentially to the life span in worms. Taken together, these results indicate that the AnkB peptide can inhibit autophagy activity in a spatially and temporally specific manner in *C. elegans*.

Discussion

In this study, we discovered that the giant isoforms of AnkB and AnkG each contain an extended LIR motif with different sequences. The AnkB-LIR peptide binds to all Atg8 members with super-strong affinities, and thus the peptide can be used as a potent and nonselective autophagy inhibitor targeting all Atg8 proteins. To our knowledge, no previous methods or tools were available to potently and selectively target certain members of the Atg8 family. The GABARAP-selective AnkG ER peptide developed here may be a useful tool for selectively inhibiting autophagy processes specifically mediated by GABARAPs with minimal perturbations to LC3s-mediated autophagy. We also provide evidence that the AnkB/G-LIR peptides, which bind to mammalian Atg8s with super-strong affinities, also inhibit the function of the GABARAP ortholog in *C. elegans*. The AnkB/G-LIR peptides developed in this study may be used in other animal systems to inhibit all steps of Atg8-mediated autophagy by nonselectively targeting all Atg8s with the AnkB-LIR peptide or selectively targeting the GABARAPs with the AnkG ER peptide.

Since the AnkB/G-LIR peptides are genetically encodable, one can easily control the expression of the peptides in living animals in essentially any tissues of interest and at any time point during the life span. This provides a powerful mean for investigating the functions of Atg8s and specifically Atg8-mediated autophagy under very broad physiological and pathological conditions in diverse organisms, including humans. Taking *C. elegans* as an example, autophagy is important to a variety of developmental processes⁴¹. Several RNAi-based methods have been developed to achieve tissue-specific gene knockdown in *C. elegans*. RNAi knockdown of most autophagy genes, delivered by either injection or RNAi feeding, is not as effective as and causes less severe defects than those seen autophagy mutants. RNAi efficiency varies among animals and also has limitations for genetic manipulations. Compared to RNAi inactivation assays, overexpression of the super-potent AnkB peptide offers several advantages. The block in autophagy caused by the AnkB peptide does not involve ATG protein turnover and RNA degradation. Compared to RNAi inactivation of autophagy genes, the autophagy defect caused by overexpression of the AnkB peptide is much more severe in many tissues. Overexpression of the super-potent AnkB peptide causes accumulation of protein aggregates in many tissues comparable to that in null autophagy mutants. Moreover, the degree of autophagy reduction also correlates with the expression level of the AnkB WT peptide. By using different promoters for AnkB expression, autophagy activity can be blocked in a strict tissue- and time-dependent manner. Therefore, the AnkB WT peptide can be used as a powerful tool for modulating autophagy activity in a tissue- or cell-type-specific and developmental-stage-specific manner, which is essential for studying how autophagy activity is coordinately regulated in different tissues during development.

Another extension of applications of the AnkB/G-LIR peptides is to use tagged AnkB WT peptide as sensitive sensors to detect all members of the Atg8 family of proteins and to use tagged AnkG ER peptide as a specific and sensitive sensor to detect the GABARAP

subfamily Atg8s *in vitro* and in cells or tissues. We have demonstrated that the AnkB/G-LIR peptides developed in this work can be used as alternatives to antibodies against Atg8s. It would be ideal if specific and potent inhibitory peptides could be developed to bind to each individual member of the Atg8 family of proteins in the future.

Finally, it should be noted that the super-strong Atg8 binding peptides are exclusively found in the giant isoforms of AnkG and AnkB, which are specifically expressed in the axons of neurons and enriched in axon initial segment and nodes of Ranvier (for AnkG)³⁵ or distal axon regions (for AnkB)^{37,42,43}. Very little is known about the functions of the super-strong binding between the giant ankyrins and Atg8s. The only reported function is that the giant AnkG-GABARAP interaction can regulate GABA_A receptor trafficking in inhibitory synapses³⁶. It is known that both LC3- and GABARAP-subfamily Atg8 proteins are found in axons of mammalian neurons, and the levels of LC3s are quite high^{19,44}. The extreme morphology of myelinated axons and demands for keeping axons healthy for the entire life span of animals may require certain unappreciated autophagy-related processes that are not needed in other tissues. Accordingly, neurons have acquired the giant AnkB and AnkG that can bind to the Atg8 proteins with extremely strong affinities. Alternatively, it is possible that the portion of Atg8 proteins interacting with giant AnkB and AnkG have functions unrelated to autophagy. Either scenario will be an important and interesting direction for future research.

Methods

Methods, including statements of data availability and any associated accession codes and references, are available at <https://doi.org/10.1038/s41589-018-0082-8>.

Received: 28 October 2017; Accepted: 23 April 2018;
Published online: 4 June 2018

References

- De Duve, C. & Wattiaux, R. Functions of lysosomes. *Annu. Rev. Physiol.* **28**, 435–492 (1966).
- Ohsumi, Y. Historical landmarks of autophagy research. *Cell Res.* **24**, 9–23 (2014).
- Bento, C. F. et al. Mammalian autophagy: how does it work? *Annu. Rev. Biochem.* **85**, 685–713 (2016).
- Galluzzi, L. et al. Molecular definitions of autophagy and related processes. *EMBO J.* **36**, 1811–1836 (2017).
- Nakatogawa, H., Suzuki, K., Kamada, Y. & Ohsumi, Y. Dynamics and diversity in autophagy mechanisms: lessons from yeast. *Nat. Rev. Mol. Cell Biol.* **10**, 458–467 (2009).
- Choi, A. M., Ryter, S. W. & Levine, B. Autophagy in human health and disease. *N. Engl. J. Med.* **368**, 651–662 (2013).
- Galluzzi, L., Bravo-San Pedro, J. M., Levine, B., Green, D. R. & Kroemer, G. Pharmacological modulation of autophagy: therapeutic potential and persisting obstacles. *Nat. Rev. Drug Discov.* **16**, 487–511 (2017).
- Levine, B., Mizushima, N. & Virgin, H. W. Autophagy in immunity and inflammation. *Nature* **469**, 323–335 (2011).
- Menzies, F. M., Fleming, A. & Rubinsztein, D. C. Compromised autophagy and neurodegenerative diseases. *Nat. Rev. Neurosci.* **16**, 345–357 (2015).
- Tsukada, M. & Ohsumi, Y. Isolation and characterization of autophagy-defective mutants of *Saccharomyces cerevisiae*. *FEBS Lett.* **333**, 169–174 (1993).
- Mizushima, N., Yoshimori, T. & Ohsumi, Y. The role of Atg proteins in autophagosome formation. *Annu. Rev. Cell Dev. Biol.* **27**, 107–132 (2011).
- Meléndez, A. et al. Autophagy genes are essential for dauer development and life-span extension in *C. elegans*. *Science* **301**, 1387–1391 (2003).
- Ohsumi, Y. Molecular dissection of autophagy: two ubiquitin-like systems. *Nat. Rev. Mol. Cell Biol.* **2**, 211–216 (2001).
- Tian, Y. et al. *C. elegans* screen identifies autophagy genes specific to multicellular organisms. *Cell* **141**, 1042–1055 (2010).
- Shpilka, T., Weidberg, H., Pietrokovski, S. & Elazar, Z. Atg8: an autophagy-related ubiquitin-like protein family. *Genome Biol.* **12**, 226 (2011).
- Wild, P., McEwan, D. G. & Dikic, I. The LC3 interactome at a glance. *J. Cell Sci.* **127**, 3–9 (2014).

17. Nakatogawa, H., Ichimura, Y. & Ohsumi, Y. Atg8, a ubiquitin-like protein required for autophagosome formation, mediates membrane tethering and hemifusion. *Cell* **130**, 165–178 (2007).
18. Mizushima, N. et al. A protein conjugation system essential for autophagy. *Nature* **395**, 395–398 (1998).
19. Kabeya, Y. et al. LC3, a mammalian homologue of yeast Apg8p, is localized in autophagosomal membranes after processing. *EMBO J.* **19**, 5720–5728 (2000).
20. Weidberg, H. et al. LC3 and GATE-16/GABARAP subfamilies are both essential yet act differently in autophagosome biogenesis. *EMBO J.* **29**, 1792–1802 (2010).
21. Wu, F. et al. Structural basis of the differential function of the two *C. elegans* Atg8 homologs, LGG-1 and LGG-2, in autophagy. *Mol. Cell* **60**, 914–929 (2015).
22. Kraft, C. et al. Binding of the Atg1/ULK1 kinase to the ubiquitin-like protein Atg8 regulates autophagy. *EMBO J.* **31**, 3691–3703 (2012).
23. McEwan, D. G. et al. PLEKHM1 regulates autophagosome-lysosome fusion through HOPS complex and LC3/GABARAP proteins. *Mol. Cell* **57**, 39–54 (2015).
24. Wang, Z. et al. The Vici syndrome protein EPG5 is a Rab7 effector that determines the fusion specificity of autophagosomes with late endosomes/lysosomes. *Mol. Cell* **63**, 781–795 (2016).
25. Bjørkøy, G. et al. p62/SQSTM1 forms protein aggregates degraded by autophagy and has a protective effect on huntingtin-induced cell death. *J. Cell Biol.* **171**, 603–614 (2005).
26. Kirkin, V. et al. A role for NBR1 in autophagosomal degradation of ubiquitinated substrates. *Mol. Cell* **33**, 505–516 (2009).
27. Mizushima, N., Yoshimori, T. & Levine, B. Methods in mammalian autophagy research. *Cell* **140**, 313–326 (2010).
28. Klionsky, D. J. et al. Guidelines for the use and interpretation of assays for monitoring autophagy, 3rd edition. *Autophagy* **12**, 1–222 (2016).
29. Manil-Ségalen, M. et al. The *C. elegans* LC3 acts downstream of GABARAP to degrade autophagosomes by interacting with the HOPS subunit VPS39. *Dev. Cell* **28**, 43–55 (2014).
30. Noda, N. N., Ohsumi, Y. & Inagaki, F. Atg8-family interacting motif crucial for selective autophagy. *FEBS Lett.* **584**, 1379–1385 (2010).
31. Birgisdottir, A. B., Lamark, T. & Johansen, T. The LIR motif — crucial for selective autophagy. *J. Cell Sci.* **126**, 3237–3247 (2013).
32. Lee, Y. K. et al. Development of LC3/GABARAP sensors containing a LIR and a hydrophobic domain to monitor autophagy. *EMBO J.* **36**, 1100–1116 (2017).
33. Stolz, A. et al. Fluorescence-based ATG8 sensors monitor localization and function of LC3/GABARAP proteins. *EMBO J.* **36**, 549–564 (2017).
34. Kordeli, E., Lambert, S. & Bennett, V. AnkyrinG. A new ankyrin gene with neural-specific isoforms localized at the axonal initial segment and node of Ranvier. *J. Biol. Chem.* **270**, 2352–2359 (1995).
35. Jenkins, P. M. et al. Giant ankyrin-G: a critical innovation in vertebrate evolution of fast and integrated neuronal signaling. *Proc. Natl Acad. Sci. USA* **112**, 957–964 (2015).
36. Tseng, W. C., Jenkins, P. M., Tanaka, M., Mooney, R. & Bennett, V. Giant ankyrin-G stabilizes somatodendritic GABAergic synapses through opposing endocytosis of GABA_A receptors. *Proc. Natl Acad. Sci. USA* **112**, 1214–1219 (2015).
37. Chan, W., Kordeli, E. & Bennett, V. 440-kD ankyrinB: structure of the major developmentally regulated domain and selective localization in unmyelinated axons. *J. Cell Biol.* **123**, 1463–1473 (1993).
38. Olsvik, H. L. et al. FYCO1 contains a C-terminally extended, LC3A/B-preferring LC3-interacting region (LIR) motif required for efficient maturation of autophagosomes during basal autophagy. *J. Biol. Chem.* **290**, 29361–29374 (2015).
39. Cheng, X. et al. Structural basis of FYCO1 and MAP1LC3A interaction reveals a novel binding mode for Atg8-family proteins. *Autophagy* **12**, 1330–1339 (2016).
40. Maruyama, Y. et al. LC3B is indispensable for selective autophagy of p62 but not basal autophagy. *Biochem. Biophys. Res. Commun.* **446**, 309–315 (2014).
41. Zhang, H. et al. Guidelines for monitoring autophagy in *Caenorhabditis elegans*. *Autophagy* **11**, 9–27 (2015).
42. Kunimoto, M. A neuron-specific isoform of brain ankyrin, 440-kD ankyrinB, is targeted to the axons of rat cerebellar neurons. *J. Cell Biol.* **131**, 1821–1829 (1995).
43. Galiano, M. R. et al. A distal axonal cytoskeleton forms an intra-axonal boundary that controls axon initial segment assembly. *Cell* **149**, 1125–1139 (2012).
44. Fu, M. M., Nirschl, J. J. & Holzbaur, E. L. F. LC3 binding to the scaffolding protein JIP1 regulates processive dynein-driven transport of autophagosomes. *Dev. Cell* **29**, 577–590 (2014).

Acknowledgements

We thank the BL19U1 beamline at National Facility for Protein Science Shanghai (NFPS) and BL17U1 beamline at Shanghai Synchrotron Radiation Facility (SSRF) for X-ray beam time, and staff at the BioCRF of HKUST for assistance in MALDI-TOF analysis. The GFP-LC3-expressing HeLa stable cell line was a kind gift from Yingyu Chen, Peking University School of Basic Medical Sciences. This work was supported by National Key R&D Program of China (2016YFA0501903) and a 973 program grant (2014CB910204) from the Minister of Science and Technology of China to M.Z., grants from RGC of Hong Kong (664113, 16103614, 16100517 and AoE-M09-12) to M.Z., and grants from the National Natural Science Foundation of China (NSFC) (31421002, 31630048, 31561143001 to H.Z. and 31670734 to C.W.). C.W. is supported by CAS Pioneer Hundred Talents Program. M.Z. is a Kerry Holdings Professor in Science and a Senior Fellow of IAS at HKUST.

Author contributions

J.L., R.Z., C.W. and K.C. performed structural and biochemical experiments; H. Zheng, H. Zhao and C.Y. performed worm experiments; R.Z. performed COS7 cell experiments; J.L., C.W., H. Zhang and M.Z. wrote the paper, and all authors approved the manuscript; H. Zhang and M.Z. supervised the research; M.Z. coordinated the project.

Competing interests

The authors declare no competing interests.

Additional information

Supplementary information is available for this paper at <https://doi.org/10.1038/s41589-018-0082-8>.

Reprints and permissions information is available at www.nature.com/reprints.

Correspondence and requests for materials should be addressed to H.Z. or C.W. or M.Z.

Publisher's note: Springer Nature remains neutral with regard to jurisdictional claims in published maps and institutional affiliations.

Methods

Constructs, protein expression and purification. The coding sequences of the GABARAP (UniProt: Q9DCD6), GABARAPL1 (UniProt: Q8R3R8), GABARAPL2 (UniProt: P60521), LC3A (UniProt: Q91VR7), and LC3B (UniProt: Q9CQV6) constructs were PCR amplified from mouse muscle or brain cDNA libraries. The coding sequence of human LC3C (UniProt: Q9BXW4) was a generous gift from Lifeng Pan (Shanghai Institute of Organic Chemistry, CAS, China). The coding sequence of AnkG-LIR construct was PCR amplified from the full-length rat 270 kDa AnkG (UniProt: O70511) template, which was a kind gift from Vann Bennett (Duke University, USA). The coding sequences of human AnkB-LIR (UniProt: Q01484) and FAM134B-LIR (UniProt: Q9H6L5) constructs were PCR amplified from synthetic oligonucleotides. All point mutations were created using the QuikChange site-directed mutagenesis kit and confirmed by DNA sequencing. All constructs used for protein expression were cloned into a home-modified pET32a vector. All constructs used for heterologous cells transfection were cloned into a p-mCherry-C1 vector. Recombinant proteins were expressed in BL21 (DE3) *Escherichia coli* cells with induction by 0.25 mM IPTG at 16°C. The N-terminal Trx-His₆-tagged proteins were purified using a Ni²⁺-NTA agarose affinity column followed by size-exclusion chromatography (Superdex 200 column from GE Healthcare) in a final buffer containing 100 mM NaCl, 50 mM Tris-HCl (pH 7.8), 1 mM DTT and 1 mM EDTA. The purities and molecular weights were verified by SDS-PAGE. For crystallization of the AnkB complexes, the chemically synthesized AnkB peptide was used and the purity and molecular weight were verified by HPLC and mass spectrometry. For the dot blot and the peptide fluorescent labeling experiment, a commercially synthesized 5-TAMRA conjugated peptide was used. All concentrations for the unlabeled peptide were determined by absorbance at 280 nm. For the fluorescently labeled peptide, in addition to absorbance at 280 nm, absorbance at 555 nm was also used to calculate an accurate concentration. The *n* values representing the binding ratios derived from the ITC experiments also help to verify the concentrations determined UV absorption. The sequences of the peptides used in this study and their purities are summarized in Supplementary Table 5.

Isothermal titration calorimetry assay. Isothermal titration calorimetry (ITC) measurements were carried out on a VP-ITC Microcal calorimeter (Malvern) at 25°C. Titration buffer contained 50 mM Tris-HCl, pH 7.8, 100 mM NaCl, 1 mM DTT and 1 mM EDTA. For a typical experiment, each titration was performed by injecting a 10 μ L aliquot of protein sample (200–400 μ M) into the cell containing another reactant (20–40 μ M) at a time interval of 120 s to ensure that the titration peak returned to the baseline. Altogether, 27 aliquots were titrated in each individual experiment. For the competition experiments, proteins in the syringe were titrated to a mixture of a twofold molar concentration excess of competitors over the reactants in the cell. The titration data were analyzed with Origin7.0 using a one-site binding or competitive binding model.

Crystallography. All crystals were obtained by hanging drop or sitting drop vapor diffusion methods at 16°C. Crystals of AnkG-LIR-GABARAPL1 were grown in solution containing 35% w/v pentaerythritol ethoxylate 797 (15/4 EO/OH), 0.2 M ammonium sulfate and 0.1 M sodium acetate (pH 4.6); crystals of AnkG-LIR-LC3B were grown in solution containing 10% v/v 2-propanol, 0.2 M zinc acetate and 0.1 M MES buffer (pH 6.5); crystals of AnkB-LIR-GABARAP were grown in solution containing 12% w/v PEG3350, 5 mM CoCl₂, 5 mM NiCl₂, 5 mM CdCl₂, 5 mM MgCl₂ and 0.1 M HEPES buffer (pH 7.5); crystals of AnkB-LIR-LC3B were grown in solution containing 2.4 M ammonium phosphate dibasic and 0.1 M Tris buffer (pH 8.5). Before diffraction experiments, crystals were soaked in the original crystallization solutions (for AnkG-LIR-GABARAPL1) or the corresponding crystallization solutions containing an additional 20% glycerol (for the other three) for cryoprotection. All datasets were collected at the Shanghai Synchrotron Radiation Facility BL17U1 or BL19U1 beamline at 100 K and a wavelength of 0.9793 Å (for AnkG-LIR-LC3B and AnkB-LIR-LC3B) or 0.9777 Å (for AnkG-LIR-GABARAPL1 and AnkB-LIR-GABARAP). Data were processed and scaled using HKL2000 or HKL3000⁴⁵.

Structures were solved by molecular replacement using PHASER⁴⁶ with the apo-form structures of GABARAP, GABARAPL1 and LC3B (PDB: 1KJT, 2R2Q and 1UGM, respectively) as the searching models. Peptides were manually built according to the $F_o - F_c$ difference maps in COOT⁴⁷. Further manual model adjustment and refinement were completed iteratively using COOT⁴⁷ and PHENIX⁴⁸ or Refmac⁴⁹. The final models were validated by MolProbity⁵⁰, and statistics are summarized in Supplementary Table 1. For the final model of AnkG-LIR-GABARAPL1, 96.5% and 3.5% of the residues were in the favored and allowed regions of the Ramachandran plot, respectively; for the final model of AnkG-LIR-LC3B, 98.4% and 1.6% of the residues were in the favored and allowed regions; for the final model of AnkB-LIR-GABARAP, 98.7% and 1.3% of the residues were in the favored and allowed regions; for the final model of AnkB-LIR-LC3B, 98.9% and 1.1% of the residues were in the favored and allowed regions. All structure figures were prepared using PyMOL (<http://www.pymol.org/>).

Cell culture, transfection and starvation. COS7 cells were cultured on 35 mm dishes with 10 mm diameter uncoated glass bottom (MatTek) in DMEM (HyClone,

SH30022.01B) with 10% FBS (HyClone, SH30084.03) supplemented with 50 μ g/mL penicillin-streptomycin. Cells were incubated at 37°C with 5% CO₂. Around 18 h after being seeded onto the dishes, the cells reached ~50% confluency. Cells were then transfected with 500 ng plasmids using Lipofectamine 2000 transfection reagent (Invitrogen, 11668019) following the protocol suggested by the manufacturer. Around another 18 h after transfection, cells were exposed to starvation. For serum starvation, cells were rinsed three times with PBS and incubated in DMEM without FBS or amino acids (HyClone, customized) at 37°C for 3 h. For EBSS starvation, cells were rinsed three times with PBS and incubated in EBSS (containing 1.0 g/L glucose; Gibco, 14155-063) at 37°C for 3 h. For experiments assessing GABARAP-positive puncta, similar procedures to those described above were adopted, except that different brands of reagents were used: cell culture: DMEM (Gibco, 12800-017), FBS (HyClone, SH30070.03); transfection: ViaFect (Promega, E4981). Additionally, the starvation medium was supplemented with 30 μ M chloroquine (Sigma, C6628) in GABARAP puncta assessment experiments. The cell line used in this study was not further authenticated and not found to be on the list of commonly misidentified cell lines (International Cell Line Authentication Committee). Cells tested negative for mycoplasma contamination by cytoplasmic DAPI staining.

Immunostaining and antibodies. COS7 cells were cultured, transfected and starved as described above. Before immunostaining, cells were first rinsed with PBS three times and then fixed in 4% paraformaldehyde at room temperature for 15 min, followed by 10 min at room temperature for permeabilization with 0.2% Triton X-100 (100 μ g/mL digitonin (Sigma, D141) in DMSO for LC3 antibody). After blocking with 5% goat serum for 60 min at room temperature, cells were incubated with primary antibodies diluted in 5% goat serum for overnight at 4°C. On the next day, cells were rinsed three times (10 min each) with PBS and stained with fluorescently labeled secondary antibodies for 1.5 h at room temperature. After another three washes with PBS, dishes were then mounted with mounting medium supplemented with DAPI (Vector Laboratories, H-1200) before imaging. For experiments assessing GABARAP-positive puncta, similar procedures to those described above were adopted, except that the blocking goat serum was substituted with donkey serum. The following antibodies were used in this study: anti-LC3B (1:200, MBL, M152-3), anti-p62 (1:200, MBL, PM045), anti-GABARAP (1:400, Cell Signaling, 13733); all secondary antibodies were purchased from Life Technologies (donkey anti-Mouse, Alexa Fluor 594, Cat#A-21203; donkey anti-Mouse, Alexa Fluor 488, Cat#A-21202; donkey anti-Rabbit, Alexa Fluor 594, Cat#A-21207; donkey anti-Rabbit, Alexa Fluor 488, Cat#A-21206) or Jackson ImmunoResearch (goat anti-Mouse, DyLight 405, Cat#115-475-003, goat anti-Rabbit, DyLight 405, Cat#111-475-003).

Microscopy and data analysis. All cell culture images were acquired with a Zeiss LSM 880 laser-scanning confocal microscope. Images were captured using a 40 \times 1.4 oil objective with pinhole setting of 1 Airy unit and zoom factor setting of 1.8 \times . The images were then analyzed with ImageJ software (<http://imagej.nih.gov/ij/>). All puncta were manually counted.

Dot blot and antibodies. Purified GABARAP, LC3B and thioredoxin (Trx) proteins were stored in a buffer containing 100 mM NaCl, 50 mM Tris-HCl, pH 7.8, 1 mM EDTA and 1 mM DTT. Proteins were first diluted to 177 μ M (3rd nM) using the same buffer and then underwent serial dilution by factors of 3 to reach the final concentration of 1 nM (3rd nM). 2 μ L of the diluted proteins were pipetting directly onto a nitrocellulose membrane (Bio-Rad). After drying at room temperature, the membrane was blocked in PBS with 5% milk for 1 h followed by incubation for 1 h at room temperature with either primary antibody or 1 μ M fluorescently labeled peptide. The membrane was then washed with PBS containing 0.1% Tween-20 three times. For the fluorescently labeled peptide, the dot signal was visualized by Chemidoc (Bio-Rad) directly. For the antibody, the membrane was then incubated with fluorescently labeled secondary antibody and detected with the LI-Cor Odyssey 9120 Imaging System. Trx protein served as a negative control.

The following antibodies were used in this study: anti-LC3 (1:400, MBL, M152-3), anti-GABARAP (1:1,000, Cell Signaling, 13733); IRDye 680RD goat anti-mouse IgG (1:10,000, LI-Cor, P/N 925-68070); IRDye 800CW goat anti-rabbit IgG (1:10,000, LI-Cor, P/N 925-32211).

C. elegans strains. All experiments were performed at 20°C, and the following strains were used in this work: *unc-76(e911)*, *bpIs151(Psqst-1::sqst-1::gfp,unc-76)*, *bpIs193(Phlh-1::sqst-1::gfp,unc-76)*, *bpIs267(Py37a1b.5::sqst-1::gfp,unc-76)*, *bpIs262(Pges-1::sqst-1::gfp,unc-76)*, *atg-9(bp594)*, *bpEx290(Pnfya-1::mcherry::ankb wt,unc-76)*, *bpEx291(Pnfya-1::mch::ankb wt,unc-76)*, *bpEx292(Pnfya-1::mcherry::ankb wr,unc-76)*, *bpEx293(Pnfya-1::mcherry::ankb wr,unc-76)*, *bpEx294(Pmyo-3::mcherry::ankb wt,unc-76)*, *bpEx295(Pmyo-3::mcherry::ankb wt,unc-76)*, *bpEx296(Pmyo-3::mcherry::ankb wr,unc-76)*, *bpEx297(Pmyo-3::mcherry::ankb wr,unc-76)*, *bpEx298(Pvha-6::mcherry::ankb wt,unc-76)*, *bpEx299(Pvha-6::mcherry::ankb wt,unc-76)*, *bpEx300(Pvha-6::mcherry::ankb wr,unc-76)*, *bpEx301(Pvha-6::mcherry::ankb wr,unc-76)*, *bpEx302(Py37a1b.5::mcherry::ankb wt,unc-76)*, *bpEx303(Py37a1b.5::mcherry::ankb wt,unc-76)*, *bpEx304(Py37a1b.5::mcherry::ankb wr,unc-76)*, *bpEx305(Py37a1b.5::mcherry::*

ankb wr,unc-76), *bpEx306(Pnfya-1::mcherry::ankb wt,rol-6)*, *bpEx307(Pnfya-1::mcherry::ankb wr,rol-6)*, *bpEx308(Pmyo-3::mcherry::ankb wt,rol-6)*, *bpEx309(Pmyo-3::mcherry::ankb wr,rol-6)*, *bpEx310(Pvha-6::mcherry::ankb wt,rol-6)*, *bpEx311(Pvha-6::mcherry::ankb wr,rol-6)*, *bpEx312(Py37a1b.5::mcherry::ankb wt,rol-6)*, *bpEx313(Py37a1b.5::mcherry::ankb wr,rol-6)*, *bpEx314(Py37a1b.5::mcherry::ankg wt,rol-6)*, *bpEx315(Py37a1b.5::mcherry::ankg er,rol-6)*, *bpEx316(Py37a1b.5::mcherry::ankg wr,rol-6)*, *bpEx317(Pcol-19::mcherry::ankb wt,rol-6)* and *bpEx318(Pmyo-3::mcherry::ankb wt,rol-6)*.

Plasmid construction for *C. elegans* experiments. DNA sequences encoding mCherry::AnkB WT, mCherry::AnkB WR, mCherry::AnkG WT, mCherry::AnkG WR and mCherry::AnkG ER were cloned into vectors containing different promoters. The following promoters were used in this study: *nfy-1* for whole animal expression, *myo-3* and *hlh-1* for body wall muscle cells, *vha-6* and *ges-1* for intestinal cells and *y37a1b.5* for hypodermal cells.

To determine autophagic degradation of SQST-1::GFP, the plasmid expressing mCherry::AnkB WT or mCherry::AnkB WR was injected into *bpIs151* worms (at a concentration of 100 ng/μL), *bpIs193* worms (30 ng/μL for high expression level and 1 ng/μL for low expression level), *bpIs262* worms (60 ng/μL) or *bpIs267* worms (100 ng/μL). *pRF4(rol-6[*su1006*])* (50 ng/μL) was used as a co-injection marker. At least two transgenic lines were analyzed for each construct.

Hatch rate, growth rate and life span assay. The constructs expressing AnkB WT or AnkB WR driven by different promoters were co-injected with *unc-76* expression vector (50 ng/μL) into *unc-76(e911)* animals. Transgenic animals expressing AnkB WT and AnkB WR with similar Cherry intensities were analyzed.

Hatch rate. Fifty to 100 well-fed Cherry-positive adult animals were transferred to a new plate to lay embryos for 2 h. Cherry-positive embryos were picked to a new plate and the number was counted; this number was used as the denominator. After 72 h, Cherry-positive L4 and adult worms were counted and the hatching rate was calculated. The experiment was performed at least three times.

Developmental time. Fifty to 100 well-fed Cherry-positive young adult animals were transferred to a new plate to lay embryos for 1 h. Cherry-positive embryos were then transferred singly to new plates. Time for embryos to develop into L1 larvae or into young adults was recorded.

Life span assay. Eighty to 100 L4 animals were transferred to five fresh NGM plates with 15 mM FUDR. Worms were scored every day or every second day for survival. Animals were scored as dead if they failed to respond to gentle touches on the body, head and tail with a worm pick. Worms that crawled off the plate or showed ruptured vulvae were omitted from analysis. At least three independent experiments were performed for each genotype. OASIS 2 (Online Application for Survival Analysis 2, <https://sbi.postech.ac.kr/oasis2/>) and GraphPad Prism 5 were used for statistical analysis. The log-rank (Mantel-Cox) method was used to calculate *P* values.

Statistical analysis. For the LC3-, GABARAP- and p62-positive puncta quantification, data were expressed as mean ± s.e.m. and statistically analyzed with GraphPad Prism 6 using one-way ANOVA followed by Tukey's multiple comparisons test. Three independent experiments for LC3 puncta analysis: AnkB WT, 60 cells; AnkB WR, 44 cells; AnkG WT, 58 cells; AnkG WR, 51 cells; AnkG ER, 61 cells; mCherry, 57 cells. Three independent experiments for GABARAP puncta analysis: AnkB WT, 139 cells; AnkB WR, 162 cells; AnkG WT, 153 cells; AnkG WR, 176 cells; AnkG ER, 138 cells; mCherry, 160 cells. Four independent experiments for p62 puncta analysis: AnkB WT, 89 cells; AnkB WR, 61 cells; AnkG WT, 74 cells; AnkG WR, 81 cells; AnkG ER, 77 cells; mCherry, 81 cells.

For the hatch rate and developmental time experiments in *C. elegans*, data are shown as mean ± s.d. Two-tailed unpaired Student's *t*-test was performed for statistical analysis. Four independent experiments were performed for analysis of hatch rate: *Pnfya-1::ch::AnkB WT* (*n* = 236) and *Pnfya-1::ch::AnkB WR* (*n* = 207). Three independent experiments were performed for analysis of developmental time: *Pnfya-1::ch::AnkB WT* (*n* = 13) and *Pnfya-1::ch::AnkB WR* (*n* = 14).

Imaging, quantification and statistical analysis for SQST-1::GFP aggregates. Images were taken using a Zeiss Axio Imager M2 microscope. Comparable images of animals were captured at the same developmental stage and similar region with the same exposure time and magnification. Five independent animals for each strain were used for quantification assay. The number and fluorescence intensity of SQST-1::GFP aggregates were quantified using ImageJ software. Two-tailed unpaired Student's *t*-test was performed for statistical analysis and results shown as mean ± s.d.

RNA interference (RNAi) in worms. RNAi bacteria were cultured on NGM agar plates containing 1 mM IPTG. Synchronized L1 worms contain *bpIs267* (*Phyp7::sqst-1::gfp*) were plated onto RNAi feeding plates and F1 were analyzed for SQST-1::GFP accumulation phenotype. All RNAi clones were confirmed by sequencing.

Electron microscopy. COS7 cells were transfected with mCherry-AnkB WT and mCherry-AnkB WR for 72 h. mCherry-positive cells were sorted by flow cytometry (BD FACSAria IIIu). Collected cells were fixed with 2.5% glutaraldehyde in PBS overnight at 4 °C. After 3 washes in PBS, cells were postfixed in 1% OsO₄ and 0.05% potassium ferrocyanide for 45 min. Cells were then washed with water and dispersed in thiocarbonylhydrazide solution for 30 min at room temperature. Cells were then washed again and incubated with 1% OsO₄ for 45 min at room temperature. After washing, cells were further dehydrated with a graded series of ethanol solutions and embedded in epoxy resin. A 120-kV electron microscope (H-7650B, Hitachi) was used at 80 kV. Images were captured with an AMT CCD camera (XR-41) using Digital Micrograph software.

Reporting Summary. Further information on experimental design is available in the Nature Research Reporting Summary linked to this article.

Data availability. Atomic coordinates and structure factors are available from the Protein Data Bank under accession codes PDB 5YIP (AnkG/GABARAPL1), 5YIQ (AnkG/LC3B), 5YIR (AnkB/GABARAP) and 5YIS (AnkB/LC3B).

References

- Otwinowski, Z. & Minor, W. Processing of X-ray diffraction data collected in oscillation mode. *Methods Enzymol.* **276**, 307–326 (1997).
- McCoy, A. J. et al. Phaser crystallographic software. *J. Appl. Crystallogr.* **40**, 658–674 (2007).
- Emsley, P., Lohkamp, B., Scott, W. G. & Cowtan, K. Features and development of Coot. *Acta Crystallogr. D Biol. Crystallogr.* **66**, 486–501 (2010).
- Adams, P. D. et al. PHENIX: a comprehensive Python-based system for macromolecular structure solution. *Acta Crystallogr. D Biol. Crystallogr.* **66**, 213–221 (2010).
- Murshudov, G. N. et al. REFMAC5 for the refinement of macromolecular crystal structures. *Acta Crystallogr. D Biol. Crystallogr.* **67**, 355–367 (2011).
- Chen, V. B. et al. MolProbity: all-atom structure validation for macromolecular crystallography. *Acta Crystallogr. D Biol. Crystallogr.* **66**, 12–21 (2010).

Life Sciences Reporting Summary

Nature Research wishes to improve the reproducibility of the work that we publish. This form is intended for publication with all accepted life science papers and provides structure for consistency and transparency in reporting. Every life science submission will use this form; some list items might not apply to an individual manuscript, but all fields must be completed for clarity.

For further information on the points included in this form, see [Reporting Life Sciences Research](#). For further information on Nature Research policies, including our [data availability policy](#), see [Authors & Referees](#) and the [Editorial Policy Checklist](#).

▶ Experimental design

1. Sample size

Describe how sample size was determined.

No statistical methods were used to determine the samples sizes. Our sample sizes are similar to those generally employed in the field, and as extensively used in our past studies in worm genetics. For cell culture and in vivo experiments, three or more biological replicates were typically used. For biochemical experiments, at least two replicates are used to confirm repeatability of quantitative binding results.

2. Data exclusions

Describe any data exclusions.

No data were excluded from the analyses.

3. Replication

Describe whether the experimental findings were reliably reproduced.

All attempts at replication were successful.

4. Randomization

Describe how samples/organisms/participants were allocated into experimental groups.

Samples were groups according to plasmid transfected (for cell lines) or strains (for *C. elegans*).

5. Blinding

Describe whether the investigators were blinded to group allocation during data collection and/or analysis.

No blinding was used during data acquisition and analysis due to the obvious differences among groups.

Note: all studies involving animals and/or human research participants must disclose whether blinding and randomization were used.

6. Statistical parameters

For all figures and tables that use statistical methods, confirm that the following items are present in relevant figure legends (or in the Methods section if additional space is needed).

n/a Confirmed

- The exact sample size (*n*) for each experimental group/condition, given as a discrete number and unit of measurement (animals, litters, cultures, etc.)
- A description of how samples were collected, noting whether measurements were taken from distinct samples or whether the same sample was measured repeatedly
- A statement indicating how many times each experiment was replicated
- The statistical test(s) used and whether they are one- or two-sided (note: only common tests should be described solely by name; more complex techniques should be described in the Methods section)
- A description of any assumptions or corrections, such as an adjustment for multiple comparisons
- The test results (e.g. *P* values) given as exact values whenever possible and with confidence intervals noted
- A clear description of statistics including central tendency (e.g. median, mean) and variation (e.g. standard deviation, interquartile range)
- Clearly defined error bars

See the web collection on [statistics for biologists](#) for further resources and guidance.

► Software

Policy information about [availability of computer code](#)

7. Software

Describe the software used to analyze the data in this study.

Graphpad Prism 5 & 6; OASIS 2; Origin 7.0; ImageJ 1.50b; Digital Micrograph.

For manuscripts utilizing custom algorithms or software that are central to the paper but not yet described in the published literature, software must be made available to editors and reviewers upon request. We strongly encourage code deposition in a community repository (e.g. GitHub). *Nature Methods* [guidance for providing algorithms and software for publication](#) provides further information on this topic.

► Materials and reagents

Policy information about [availability of materials](#)

8. Materials availability

Indicate whether there are restrictions on availability of unique materials or if these materials are only available for distribution by a for-profit company.

The DMEM without FBS and amino acids for serum starvation were customized made by Hyclone. No restrictions on availability of unique materials.

9. Antibodies

Describe the antibodies used and how they were validated for use in the system under study (i.e. assay and species).

For staining (Fig. 4&Supplementary Fig. 12c): anti-LC3B (1:200, MBL, M152-3), anti-p62 (1:200, MBL, PM045), anti-GABARAP (1:400, Cell Signaling, #13733)
For dot blot (Supplementary Fig. 12b): IRDye® 680RD Goat anti-Mouse IgG (1:10000, LI-Cor, P/N 925-68070); IRDye® 800CW Goat anti-Rabbit IgG (1:10000, LI-Cor, P/N 925-32211).

All primary antibodies are widely used in the field, see citations in the manufacturer's website (anti-LC3B: <https://www.mblintl.com/products/m152-3>; anti-p62: <https://www.mblintl.com/products/pm045>; anti-GABARAP: <https://www.cellsignal.com/products/primary-antibodies/gabarap-e1j4e-rabbit-mab/13733>)

10. Eukaryotic cell lines

a. State the source of each eukaryotic cell line used.

COS7: ATCC.

b. Describe the method of cell line authentication used.

The cell line used in this study was not further authenticated.

c. Report whether the cell lines were tested for mycoplasma contamination.

Cells were tested negative for mycoplasma contamination by cytoplasmic DAPI staining.

d. If any of the cell lines used are listed in the database of commonly misidentified cell lines maintained by [ICLAC](#), provide a scientific rationale for their use.

The cell line used was not found to be on the list of commonly misidentified cell lines (International Cell Line Authentication Committee).

► Animals and human research participants

Policy information about [studies involving animals](#); when reporting animal research, follow the [ARRIVE guidelines](#)

11. Description of research animals

Provide details on animals and/or animal-derived materials used in the study.

The study used wild isolates and mutants of *Caenorhabditis elegans*. Mutant worm strains were generated in the lab. Detailed strains are listed below:
 unc-76(e911), bpls151(Psqst-1::sqst-1::gfp, unc-76), bpls193(Phlh-1::sqst-1::gfp, unc-76), bpls267(Py37a1b.5::sqst-1::gfp, unc-76), bpls262(Pges-1::sqst-1::gfp, unc-76), atg-9(bp594), bpEx290(Pnfya-1::mcherry::ankb wt,unc-76), bpEx291(Pnfya-1::mcherry::ankb wt,unc-76), bpEx292(Pnfya-1::mcherry::ankb wr,unc-76), bpEx293(Pnfya-1::mcherry::ankb wr,unc-76), bpEx294(Pmyo-3::mcherry::ankb wt,unc-76), bpEx295(Pmyo-3::mcherry::ankb wt,unc-76), bpEx296(Pmyo-3::mcherry::ankb wr,unc-76), bpEx297(Pmyo-3::mcherry::ankb wr,unc-76), bpEx298(Pvha-6::mcherry::ankb wt,unc-76), bpEx299(Pvha-6::mcherry::ankb wt,unc-76), bpEx300(Pvha-6::mcherry::ankb wr,unc-76), bpEx301(Pvha-6::mcherry::ankb wr,unc-76), bpEx302(Py37a1b.5::mcherry::ankb wt,unc-76), bpEx303(Py37a1b.5::mcherry::ankb wt,unc-76), bpEx304(Py37a1b.5::mcherry::ankb wr,unc-76), bpEx305(Py37a1b.5::mcherry::ankb wr,unc-76), bpEx306(Pnfya-1::mcherry::ankb wt,rol-6), bpEx307(Pnfya-1::mcherry::ankb wr,rol-6), bpEx308(Pmyo-3::mcherry::ankb wt,rol-6), bpEx309(Pmyo-3::mcherry::ankb wr,rol-6), bpEx310(Pvha-6::mcherry::ankb wt,rol-6), bpEx311(Pvha-6::mcherry::ankb wr,rol-6), bpEx312(Py37a1b.5::mcherry::ankb wt,rol-6), bpEx313(Py37a1b.5::mcherry::ankb wr,rol-6), bpEx314(Py37a1b.5::mcherry::ankg wt,rol-6), bpEx315(Py37a1b.5::mcherry::ankg er,rol-6), bpEx316(Py37a1b.5::mcherry::ankg wr,rol-6), bpEx317(Pcol-19::mcherry::ankb wt,rol-6), bpEx318(Pmyo-3::mcherry::ankb wt,rol-6)

Policy information about [studies involving human research participants](#)

12. Description of human research participants

Describe the covariate-relevant population characteristics of the human research participants.

The study did not involve human research participants.